Intergrain and intragrain currents in bulk melt-grown $YBa_2Cu_3O_{7-\delta}$ rings

A. B. Surzhenko,* M. Zeisberger, T. Habisreuther, and W. Gawalek
Institut für Physikalische Hochtechnologie, Winzerlaer Str. 10, Jena D-07745, Germany

L. S. Uspenskaya
Institute of Solid State Physics, Russian Academy of Science, Institutskii pr. 16, Chernogolovka, Moscow District, 142432, Russia
(Received 20 December 2002; revised manuscript received 20 March 2003; published 7 August 2003)

A simple contactless method suitable for discerning between the intergrain (circular) current, which flows in the thin superconducting ring, and the intragrain current, which does not cross the weakest link, has been proposed. At first, we show that the intergrain current may directly be estimated from the magnetic flux density $B(\pm z_0)$ measured by the Hall sensor positioned in the special points $\pm z_0$ above or below the ring center. The experimental and numerical techniques to determine the value z_0 are discussed. Being very promising for the characterization of a current flowing across the joints in welded YBaCuO rings (its dependences on the temperature and external magnetic field as well as the time dissipation), the approach has been applied to study the corresponding properties of the intragrain and intergrain currents flowing across the *a*-twisted grain boundaries which are frequent in bulk melt-textured (MT) YBaCuO samples. We present experimental data related to the flux penetration inside a bore of MT YBaCuO rings both in the nonmagnetized, virgin state, and during the field reversal. The shielding properties and their dependence on external magnetic fields are also studied. Besides, we consider flux creep effects and their influence on the current redistribution during a dwell.

DOI: 10.1103/PhysRevB.68.064504 PACS number(s): 74.72.Bk, 74.25.Sv, 74.25.Ha

I. INTRODUCTION

The unique feature of thin superconducting rings has to be well known to anyone who ever tried to investigate the intergrain currents flowing across weak links in polycrystalline $YBa_2Cu_3O_{7-\delta}$ (YBCO) ceramics and/or thin films.[1–4] By changing the outer R_o and the inner R_i radii of the ring, one may essentially enlarge a difference between the length scales, R_o+R_i and R_o-R_i, over which, respectively, the intergrain and intragrain currents flow. Provided that the ring is thin enough $(R_o-R_i)\ll(R_o+R_i)$, one may reliably register the magnetic flux density B induced by the intergrain, shielding the current even if the intragrain currents much exceed it.

The melt-textured (MT) growing process[5] has generally allowed one to escape an appearance of the large-angle grain boundaries (GB's) and, thereby, the current localization inside the grains. For this reason, a worldwide interest to the ringlike geometry was fading away until an idea to weld[6] MT blocks gained a respectable reputation.[7–20] Briefly, the joining procedures consist in the welding of single MT domains during a liquid-assisted process which either releases residual BaCuO oxide trapped in the MT material[8] or uses the corresponding REBCO [RE=Tm (Refs. 9–11), Yb (Refs. 12 and 16), Er (Refs. 15 and 17), Y (Refs. 7 and 20), or Y+Ag (Refs. 13, 14, and 18)] compounds melting at lower temperatures. Since these techniques were shown to produce joints capable of carrying high currents, such artificial joining opens new perspectives for the fabrication of large-scale superconducting devices (e.g., magnetic bearings, electromotors and generators, energy storage systems, etc.[21]). Their performance, though, crucially depends on the density j_w of the critical current which the weld may transmit.

Despite an obvious necessity to compare the joints obtained under different welding conditions, surprisingly few authors reported numerical values j_w. Besides, most of these estimates were obtained by resistive measurements which, because of the Ohmic losses in the current pads, are severely limited by the maximum admissible current $I_w=j_wS\lesssim 10^3$ A. Thus, these measurements are restricted both by the surface S of the weld and by its quality j_w which, in turn, imposes the lowest-temperature margin. On the other hand, prevalent contactless methods (e.g., levitation force technique,[9,19] magneto-optical image analysis,[9,17,22] scanning Hall-sensor magnetometry,[8–15] and magnetization loop studies[8,9,18,23]) are not free of ambiguities in the processing of experimental data unless, as mentioned above, the welded sample has the shape of a thin ring. In this case, the circular current throughout a ring is limited by the weakest link which is, in turn, usually associated with a joint.

Among the above-mentioned experimental techniques, scanning Hall-sensor magnetometry looks preferable. The main reason is that, having no restrictions on the size of the joints, this method is quite suitable for the characterization of the large-scale welds required for practical applications. The same feature seems also useful for other tasks to be eventually resolved. In particular, one has to study a degradation of the critical current densities from a center of large MT domains to their rims[24] and its relation to a content of the precursor mixture, the growth temperature, etc. Aside from knowledge of the best growth conditions, such studies will allow one to determine the optimum size of welded parts. The last, but not the least, argument is a widespread use of the scanning Hall-sensor systems.[8–15]

For this technique to give reliable results, the experimental data have to be properly processed. Meanwhile, most of the authors prefer to simplify the genuine distribution of cur-

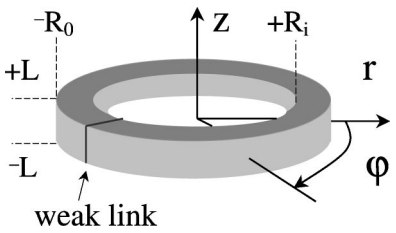

FIG. 1. Superconducting ring which contains a weak link.

rents and to consider their rings as *homogeneous* (one-turn) solenoids carrying the transport current I_w. In other words, they neglect the intragrain currents—i.e., those which do not cross the joint. We shall hereafter demonstrate that such a simplification is applicable only for rough estimates. The more accurate method—i.e., a scan of the flux trapped by a ring with its subsequent computer fit[10]—is also far from perfect. The problem is that the necessity of moving the Hall sensor makes this technique hard to exploit at different temperatures and/or external magnetic fields. Moreover, the scanning duration t_{sc} of, typically, a few minutes during which the currents may noticeably dissipate assents to start the measurements only after a long-continued dwell $t_{dw} \gg t_{sc}$. So important information about the current losses appears unavailable.

Section II of this manuscript represents simple analytical equations constituting the backbone of the novel experimental approach which combines the advantages of both methods and is free of their faults. We show that to find the densities of the intergrain and intragrain currents one does not need to waste time on the magnetic flux scan. Actually, these densities may, with proper accuracy, be estimated from two experimental points $B(r,z)$ measured at certain distances z above or below the ring center. In Sec. IV we apply this method to study the current distribution in large-scale MT YBCO rings. The results are summarized in Sec. V.

II. MODEL AND ITS SOLUTION

Let us consider a homogeneous ring (see Fig. 1) made of superconducting material with the critical current density j_m and introduce therein a weak link transmitting a current up to

$$I_w = j_w(R_o - R_i)2L = j_m f(R_o - R_i)2L, \tag{1}$$

where $f = j_w/j_m < 1$. It is worth mentioning that the weak link makes this ring *inhomogeneous* with respect to a rotation around its axis z. Let the ring was completely magnetized in strong magnetic fields applied along the z direction. The subject of our interest will be the currents flowing in the ring as well as the radial profiles $B(z=\text{const},r)$ of the vertical component of the magnetic flux density which these currents produce.

Assuming Bean's critical-state model in the simplest form of an infinitely high ($L \to \infty$) sample to be valid, one can readily outline the profile passing through the point $r=0$ and the ring area which is far enough from the weak link. Figure 2(a) shows this profile in the remanent state ($H=0$). Of

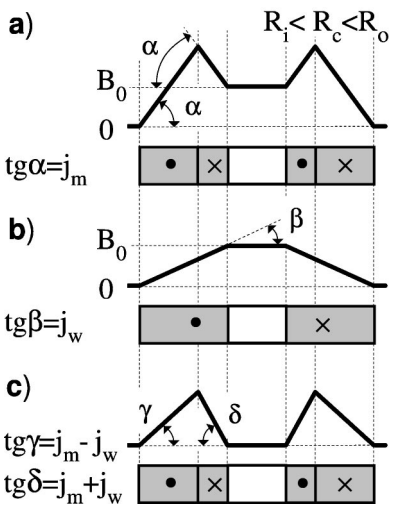

FIG. 2. Profiles of the density B of the remanent magnetic flux trapped by a ring containing weak links (a) and its components B_w and B_m induced by (b) the intergrain and (c) the intragrain currents, respectively.

necessity, this situation can readily be expanded to the case of arbitrary fields by adding a constant background $\mu_0 H$. For this reason, we shall thenceforward take into account only two components of the magnetic flux, B_w and B_m. These are induced by the intergrain current (I_w) and intragrain (I_m) current which, respectively, crosses and does not cross the weak link. When $L \to \infty$, the former results in the triangle profile truncated in the ring bore by a plateau $B_0 = j_w(R_o - R_i)$ [Fig. 2(b)], whereas the latter responds for the difference $B_m = B - B_w$ [see Fig. 2(c)]. The radius R_c wherein the intragrain current alters its direction from clockwise (CW) to counterclockwise (CCW),

$$R_c(f) = [R_o + R_i - f(R_o - R_i)]/2, \tag{2}$$

is known to change between $(R_i + R_o)/2$ at $f=0$ and R_i when $f=1$.[10] Using Eq. (2), one can calculate the amplitude

$$I_m = j_m(R_o - R_i)L(1 - f^2) \tag{3}$$

and demonstrate that the CW and CCW intragrain currents compensate each another; i.e., the current loop I_m does appear closed inside the superconducting grain.

In the case $L \to \infty$ illustrated in Fig. 2, $B_m(r < R_i) \equiv 0$; i.e., any point inside the ring bore is suitable to estimate the density $j_w = B_0/(R_o - R_i)$. This comfortable situation is, though, too far from reality. Since the finite-size rings are not free of demagnetizing effects, the term $B_m(r < R_i)$ is actually nonzero. Thus, in order to estimate the current I_w and/or its density j_w, one has to calculate and remove the component B_m from the experimentally accessible value $B(z,r)$. In this paper we solve this problem below another way. We show and gladly exploit that $B_m(z,r)$ is an alternating function: it is negative inside a certain region surrounding the ring center $(z=0, r=0)$ and positive outside it [see, for example, Fig. 4(a)]. Thus, positioning the Hall sensor somewhere at the border $B_m(z_0, r_0) = 0$, one can directly measure the inter-

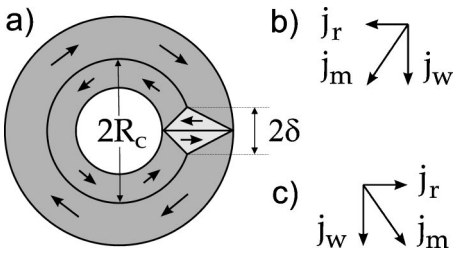

FIG. 3. (a) Currents which flow in a fully magnetized superconducting ring with a weak link and vector diagrams explaining their distribution inside the diamond-shaped area (b) above and (c) below a weak link.

grain flux component $B_w(z_0,r_0)$ and use this value to restore a ''pure'' circular current I_w flowing throughout a ring.

One could, certainly, search for a whole surface which satisfies the condition $B_m(z_0,r_0)=0$. But let us, for simplicity, restrict our search to the points along the ring axis, $r_0=0$. The magnetic flux density of a thin ($r_i=r_o=R$), one-turn solenoid at $r=0$ is well known:

$$B=\frac{I}{4L}\left[\frac{L-z}{\sqrt{R^2+(L-z)^2}}+\frac{L+z}{\sqrt{R^2+(L+z)^2}}\right]. \tag{4}$$

For finite-size rings, one requires to average the function (4) over the range between their outer r_o and inner r_i radii. Using a formal procedure $B=\int B(r)dr/\int dr$, one has a general solution

$$B=j\cdot\Phi(L,z,r_o,r_i). \tag{5}$$

Here j denotes the current density $j=I/[2L(r_o-r_i)]$ and the function Φ gives the effective size depending on four distances:

$$\Phi(L,z,r_o,r_i)=\Gamma(L-z,r_o,r_i)+\Gamma(L+z,r_o,r_i),$$

$$\Gamma(x,r_o,r_i)=\frac{x}{2}\ln\left(\frac{r_o+\sqrt{r_o^2+x^2}}{r_i+\sqrt{r_i^2+x^2}}\right). \tag{6}$$

Using these equations, one can obtain the magnetic flux densities B_w, B_m, and $B=B_w+B_m$, produced by each of three magnetic systems shown in Fig. 2 for the case of finite sizes. For example, the coil [Fig. 2(b)], which carries a current I_w of a density j_w, yields

$$B_w=j_w\Phi(L,z,R_o,R_i). \tag{7}$$

The intragrain flux component B_m is created by by a pair of coils [see Fig. 2(c)] having the same height $2L$ and the common radius R_c given by Eq. (2). Since these coils carry a current I_m of densities $j_m(1-f)$ and $-j_m(1+f)$, one has

$$B_m=K\cdot j_m[(1-f)\Phi(L,z,R_o,R_c(f))-(1+f)\Phi(L,z,R_c(f),R_i)], \tag{8}$$

where K is a geometrical factor the origin of which is illustrated in Fig. 3. One can see that a weak link is surrounded by the diamond-shaped area (marked by bright color) where

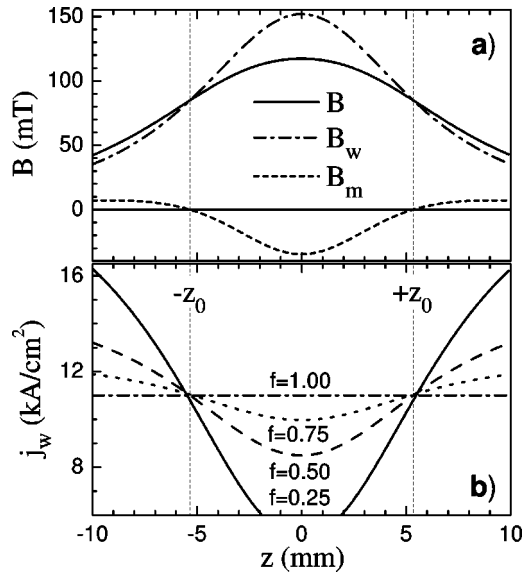

FIG. 4. (a) shows how the densities of the remanent magnetic flux B and its components B_w and B_m along the axis ($r=0$) of the ring depend on the distance z from its center, $z=0$. The ring sizes $R_o=10$ mm, $R_i=5.5$ mm, and $2L=3.8$ mm, as well as $j_w=11$ kA/cm^2 are borrowed from the work of Zheng *et al.* (Ref. 10). The missing parameter $f=j_w/j_m$ is taken to be $f=0.5$ ($j_m=22$ kA/cm^2). The j_w vs z curves in (b) are calculated from the total magnetic flux B within the one-turn approximation (7) and, thus, represent an error appearing when the term B_m is neglected.

the intragrain current I_m flows no more in the circular direction [as Eq. (5) assumes], but either toward or outward the ring center. Owing to such an arrangement, I_m within this ''diamond'' gives a negligible contribution to $B(z,r=0)$. Then, the flux density B_m of a full intragrain loop has to be corrected onto a factor $K\simeq 1-\delta/2\pi R_c$ (see Fig. 3) where the half-width δ may be estimated as the length necessary to transmit a whole current I_m given by Eq. (3). Since the radial current density j_r cannot exceed $\sqrt{j_m^2-j_w^2}$ (see the vector diagrams in Fig. 3), one can obtain

$$\delta=\frac{1}{2}(R_o-R_i)\sqrt{1-f^2} \tag{9}$$

and, then, calculate the parameter

$$K=1-N\frac{R_o-R_i}{4\pi R_c(f)}\sqrt{1-f^2} \tag{10}$$

for the case of several weak links N. This approximation is no longer valid at $N\delta>\pi R_c$—i.e., when the diamonds start to overlap each other.

In order to imagine how the flux densities vary along the ring axis, we inserted parameters of the real ring reported in Ref. 10 into Eqs. (7) and (8) and present these curves in Fig. 4(a). These data once more convince us that the one-turn approximation (7) may properly be applied to experimental values $B(z)$ only when $B_m=0$—i.e., at the points $z_0\approx\pm 5.4$ mm on the given axis ($r=0$). Otherwise, such a method may considerably underestimate ($|z|<z_0$) or overestimate ($|z|>z_0$) the current density j_w. For the parameter $f=0.5$ in Fig. 4(a), the j_w value, respectively, of the Hall

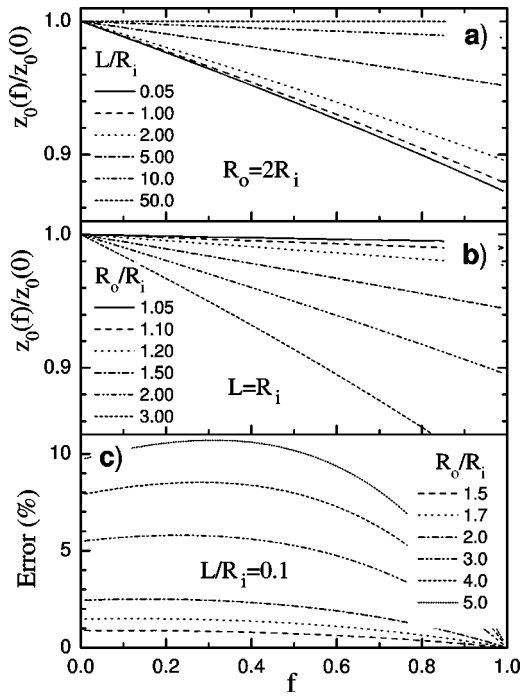

FIG. 5. (a),(b) The z_0 vs f dependences calculated from Eq. (11) at various parameters R_o, R_i, and L. (c) presents the error $B_m/B_w(z_0)$ which appears in the worse case of thick, flat rings ($R_o/R_i>1.5$, $L/R_i=0.1$) provided that the z_0 vs f dependence is neglected, namely, $z_0(f)=z_0(0)$.

sensor position $0\leqslant|z|\leqslant 10$ mm, changes in the wide range (77%–120%) around the genuine density $j_w=11$ kA/cm^2. This error essentially increases when $f\to 0$ [see Fig. 4(b)].

In order to escape such a situation, one has to know z_0. The main problem is that the expression inside the brackets in Eq. (8) depends on the unknown factor $f=j_w/j_m$ and so, certainly, does z_0 which satisfies

$$\frac{\Phi(L,z_0,R_o,R_c(f))}{\Phi(L,z_0,R_c(f),R_i)}=\frac{1+f}{1-f}. \tag{11}$$

If one could ignore this dependence, z_0 would be defined only by the ring geometry and, hence, readily calculated.

Upon a closer view at Fig. 4(b), one can really note that z_0 tends to the ring center as f increases. However, the effect seems so weak that we did not resist a temptation to know in which rings its disregard still gives an acceptable error. We studied the z_0 vs f curves at various parameters R_o, R_i, and $2L$ and revealed almost no deviation from the initial value $z_0(f=0)$ in thin ($R_i\to R_o$) and/or high ($L\to\infty$) rings [see Figs. 5(a) and 5(b)]—i.e., in those which are close to a form of ideal solenoid. As the largest deviation is, therefore, expected in thick, flat rings ($R_o\gg R_i, L\ll R_i$), it is the case to be inspected. So we calculated for such rings the amendment $B_m/B_w|_{z_0}$ which has, by the definition, to be a zero unless the z_0 vs f dependence is ignored. The points $z_0(R_i,R_o,L)=$const, wherein this ratio was estimated, were taken from Eq. (11) reduced by the substitution $f=0$ to rather comfortable form[39]

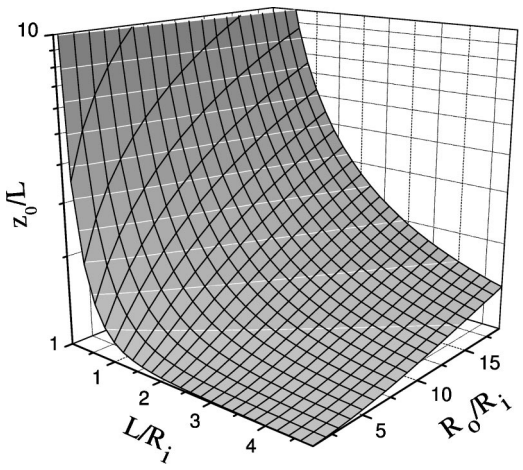

FIG. 6. The solutions of Eq. (12) normalized to the ring half-height. Note that everywhere, except for the case of an ideal solenoid ($L\to\infty, R_o/R_i\to 1$), z_0 appears outside of the ring, $|z_0|\geqslant L$. Thus, the method is not restricted by the bore diameter $2R_i$ which may be smaller than the size of the Hall-sensor holder.

$$\Phi(L,z_0,R_o,R_c(0))=\Phi(L,z_0,R_c(0),R_i), \tag{12}$$

where $R_c(0)=(R_o+R_i)/2$. Accepting the admissible error to be 2.5% and restricting, thereby [see Fig. 5(c)], the studied rings to the not too stringent condition[40] $R_o/R_i\leqslant 2$, we are qualified to use the above simplification $z_0(f)=z_0(0)$ in practice.

Thus, knowing the ring sizes (R_o, R_i, and $2L$) only, one may, on the one hand, pre-determine z_0 from Eq. (12) by numerical methods. Such solutions (normalized, for the sake of convenience, to the ring half-height L) are shown in Fig. 6. On the other hand, this numerical procedure (at least, in the case of welded rings) may *optionally* be avoided. Before joining, these rings inevitably contain one or more slits which prevent a circular current to flow ($f=0$). So the points $\pm z_0$, wherein the remanent flux density of the *cut* ring changes its sign [see Fig. 4(a)], are available for direct measurements. Then, registering $B(\pm z_0)$ above or below the center of the *welded* sample, one may readily calculate the joint quality

$$j_w=B(z_0)/\Phi(L,z_0,R_o,R_i). \tag{13}$$

Since z_0 depends only on the ring geometry, it is no matter whether the welded ring has the same j_m as that in the original material or not. This feature does look important because heating of the MT samples up to temperatures close to their melting points, which actually is the joining procedure, often results in oxygen losses and requires one to reoxygenate the samples.

III. EXPERIMENTAL DETAILS

The initial MT YBCO samples, from which we cut the rings, were grown by the top-seeding method which is described in details elsewhere.[25] Briefly, commercially purchased powders of $YBa_2Cu_3O_{7-\delta}$ and Y_2O_3 were thoroughly mixed in proportions providing the final phase

composition Y:Ba:Cu=1.5:2:3 and diluted by 1 wt% CeO_2. This mixture was uniaxially pressed into cylindrical pellets which sizes were selected to exceed the sizes of future rings. Then, a self-made $SmBa_2Cu_3O_X$ seed was installed in the center of each pellet and oriented so that its crystallographic axis *c*, [001], was parallel to the axis of cylinder. On the morrow of isothermal melt growth ($T=988\,^{\circ}C$) the samples were cooled down to room temperature and then post-annealed in flowing oxygen.

The rings were carved (by using aluminum oxide grindstones) so that the *z* axis of each ring was parallel to the *c* axis of the initial MT crystal.

The larger half of the experiments was in scanning of the *remanent* flux distribution. These scans were performed with the three-dimensional-(3D-) positioning system[26] allowing one to move the Hall sensor stepwise with a pitch of 100 μm in the horizontal plane and of 75 μm along the vertical direction. The standard procedure was the following. The rings were mounted inside a small vessel and field-cooled (FC) in magnetic fields $\mu_0 H \approx 1$ T to the liquid nitrogen temperature $T=77.3$ K. Then, the field was switched off (with a sweep rate 0.5 T/min) and a ring (still inside a vessel with a liquid nitrogen) was moved to an area available for a scan. To eliminate the undesirable scatter because of a dissipation of the remanent flux during the scanning time (typically, of a few minutes), a scan was always run after a long-continued dwell ($t_{dw}=30$ min). Both the axial $B(r=0,z)$ and radial $B(r,z=\text{const})$ profiles were studied.

To measure the hysteresis loops $B(H)$ as well as the flux dissipation $B(t)$, we mounted the Hall sensor directly on the studied ring. The Hall-sensor positioning error did not exceed 50 μm.

The magnetic moment *m* was registered by the commercial VSM (model No. 3001, Oxford Instriments Ltd). Owing to a relatively large distance between the vibrating ring and pickup coils, this value may roughly be associated with $B(z=\infty)$.

The radial flux distribution at the ring edges $z=\pm L$ in small magnetic fields ($H<3$ kOe) was also visualized by using a high-resolution magneto-optical imaging technique.[27,28]

IV. RESULTS AND DISCUSSION

In this section we report extensive experimental studies of the intergrain and intragrain currents for the ringlike geometry. At first, we investigate the current distribution in the remanent state and compare our results with those obtained by conventional methods. Then, we study the behavior of rings containing natural weak links (i.e., the boundaries between the *a*-twisted grains) in external magnetic fields. Finally, we explore the flux creep effects.

A. Cut rings in the remanent state

It is obvious that the fewer fitting parameters included in an equation, the more trustworthy one can test whether it fits an experiment or not. For this reason, we start our studies from the cut rings wherein j_m is the only parameter relevant.

TABLE I. Theoretical and experimental values z_0 in the cut rings (CR's) consisting of two 180° arcs ($N=2$). Estimates for the intragrain current density j_m are also included.

Ring No.	Ring sizes[a] (mm) R_o	R_i	$2L$	z_0 (mm) Theory	Expt.	j_m[b] (kA/cm^2)
CR1	6.05	2.95	5.35	3.92	3.70	17.9_8
CR2	6.05	2.95	4.90	3.83	3.67	18.9_8
CR3	6.05	2.95	3.98	3.60	3.52	20.2_3
CR4	6.05	2.95	3.30	3.46	3.40	21.3_4
CR5	6.05	2.95	2.81	3.37	3.34	22.6_2
CR6	6.05	2.95	2.22	3.27	3.23	22.8_3
CR7	6.05	2.95	1.55	3.20	3.21	22.9_7
CR8	4.99	2.95	1.55	2.89	2.90	22.2_3

[a]The ring sizes are given with the accuracy ± 0.03 mm.
[b]The j_m values are obtained in the self-field (remanent state) after the long-continued dwell $t_{dw}=30$ min.

When a ring contains *N* slits which obstruct the intergranular current I_w, the magnetic flux density along the ring axis ($r=0$) is given by Eq. (8) at $f=0$:

$$B=Kj_m[\Phi(L,z,R_o,R_c(0))-\Phi(L,z,R_c(0),R_i)], \quad (14)$$

where $R_c(0)$ is the average radius, $(R_o+R_i)/2$, and

$$K=1-\frac{N}{2\pi}\frac{R_o-R_i}{R_o+R_i}. \quad (15)$$

One has to note that the term in brackets totally defines the shape of the *B* vs *z* curve; i.e., j_m may change only its amplitude. Thus, estimating a disagreement between theoretical and experimental profiles $B(r=0,z)$, one can readily check to what extent our approach is to be relied upon. In particular, one can put the solutions z_0 of Eq. (12) to experimental proof. By changing the ring sizes, we can also test how j_m varies with distance from the seeding point both in the axial and in the radial directions.

For these studies we used a ring (see Table I) which was cut from the central part of the MT crystal; i.e., the ring center ($r=0$) coincided with the seeding point. The inner diameter $2R_i=5.90$ mm was selected to exceed the size (≈ 5 mm) of the Hall-sensor holder and to make, therefore, the ring suitable for a *z* scan along the whole axis $r=0$. At first, we cut this ring onto two 180° arcs and glued them together by using an epoxy resin. The toughness of such mechanical contact was good enough for a succeeding treatment of the ring by grindstones. Then, grinding, step by step, the ring bottom (i.e., reducing the ring height), we measured at each stage the axial profile $B(r=0,z)$ of the remanent flux density. During the measurements we exactly followed the procedure described in Sec. III. Some of these data are presented in Fig. 7 (open symbols). To calculate j_m for each of the rings, we used the *B* point at the ring center, $z=0$, wherein the flux density has the maximum amplitude. Thus estimated parameters j_m result in a good agreement between Eq. (14) (solid curves) and the experimental data in the whole studied range, $-8<z<8$ mm. However, a more

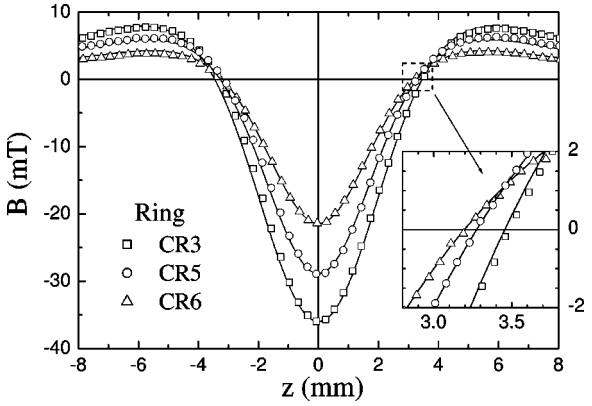

FIG. 7. The axial profiles $B(r=0,z)$ of the remanent flux density (open points) measured at $T=77.3$ K along the axis of the cut rings (see details in Table I) and their approximations (solid curves) given by Eq. (14). The inset magnifies the area around the points $B(z_0)=0$.

careful look (see Table I) reveals a certain difference. One can notice that the genuine value z_0 (estimated as the half-distance between the points wherein the experimental curve intersects the X axis) in high rings is usually a bit smaller than the z_0 predicted by Eq. (12). This feature is accompanied by the obvious tendency for j_m to decrease (from the top surface to the bottom one) and may readily be explained by the growth-related inhomogeneities of the MT material.[29,30]

In particular, the top-seeded MT crystal grows due to the motion of five habitus planes—viz., (100), $(\bar{1}00)$, (010), $(0\bar{1}0)$, and $(00\bar{1})$—which form, respectively, four *a*-growth sectors (GS's) and the *c*-GS. The latter usually has the shape of a regular pyramid with a vertex in the seeding point (see Fig. 8). During the growth the interface energy $\Delta\sigma_0$ between the $(00\bar{1})$ plane and the Y_2BaCuO_5 (Y211) inclusions appreciably differs from that for the former four habits.[29] Since $\Delta\sigma_0$ determines whether the Y211 particle with a certain size will be expelled or embraced by the solid-liquid front,[31] the volume fraction V_{211} of inclusions trapped inside the *c*-GS *always* appears much smaller than V_{211} in the *a*-GSs.[29] Meanwhile, these inclusions are well known[32] to behave as effective pinning centers. Thus, the intragrain current density j_m inside the *c*-GS has also to be less than j_m in *a*-GS's—i.e., near the crystal surface (see Fig. 8). At our growth temperature ($T=988\,^{\circ}$C) the height of the *c*-GS is approximately a half of its base.[30] So high rings ($2L \geqslant R_i$) seem to consist of the superconducting material with different j_m. Grinding the ring bottom, we gradually deleted a part with a worse j_m and, thereby, made the ring more homogeneous. One has also to mention that the j_m values in Table I are averaged over the whole height $2L$. A genuine ratio of the current density in the *a*-GS's and that in the *c*-GS may roughly be estimated as a factor of 2.0 ± 0.2 which is in good agreement with that obtained by magneto-optical methods (see, for example, Ref. 28).

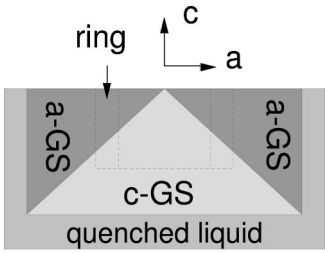

FIG. 8. The central cross section of the typical MT YBCO crystal. Note that high rings can cross the boundary between the *a* and *c* sectors grown on different habitus planes, respectively, (100) and $(00\bar{1})$.

TABLE II. The parameters of entire rings (ER's).

Ring No.	R_o	R_i	$2L$ (mm)	X	z_0	j_w [a] (kA/cm^2)	j_m [a] (kA/cm^2)	f [a]
ER1	5.00	2.90	2.60	0	2.97	13.9_5	21.6_3	0.64_5
R2	3.80	2.15	2.00	9	2.24	16.0_2	30.7_9	0.52_0
ER3	7.43	2.30	2.20	0	3.29	19.0_2	26.0_6	0.73_0
ER4	6.00	2.18	3.60	19	3.15	4.6_3	11.3_6	0.40_7

[a]The values are calculated from the $B(r=0,z)$ data measured in the remanent state after the long-continued dwell $t_{dw}=30$ min within an assumption of a single weak link ($N=1$).

We also tried to estimate the radial inhomogeneities $j_m(r)$ near the top surface of the MT crystals. For this purpose, we removed a certain portion of superconducting material from the outer periphery of the cut ring CR7 (see Table I) and revealed a vague tendency for j_m to decrease as $r\to0$.

This brief survey to the growth-induced structure of MT crystals scarcely seems redundant. At first, it confirms the validity of our results. It also gives a better understanding of why we used for further studies only homogeneous rings—i.e., those carved from the same, *a*-growth sector (see Table II). Meantime, it should not eclipse the main, to our opinion, conclusion of this section: the proposed method predicts well the ''magic position'' z_0, where the magnetic flux is free of the intragrain contribution B_m.

B. Entire rings in the remanent state

In this section we shall report experimental data for entire rings which consist of the *a*-twisted subgrains. Such subgrains are formed due to mechanical stresses which the YBCO skeleton undergoes when the growth front engulfes the Y_2BaCuO_5 inclusions. These stresses result in dislocations which, unfortunately, have a destructive tendency to amalgamate into the GB's.[29] As these stresses accrue during the growth, the misorientation angle between the neighboring subgrains (which are usually elongated along the growth direction, i.e., along either the *a* or *c* axis) gradually increases with distance from the seeding point.[29] This angle, for large enough samples, can exceed the critical limit when the GB turns into the weak link.[33–35] Having the opportunity to determine whether this limit is approached or not, we grew few extra-large ($52\times52\times25$ mm^3) MT crystals and cut entire rings from their various parts. So aside from standard ring parameters (i.e., the inner R_i and the outer R_o radii as well as the full height $2L$), we shall hereafter introduce

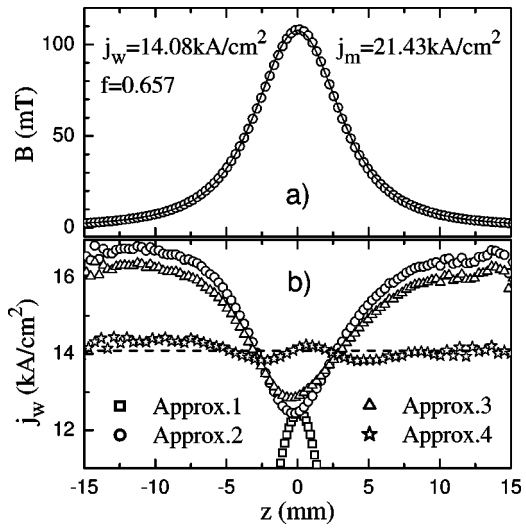

FIG. 9. (a) Variation of the remanent flux density $B(r=0,z)$ along the axis of the ring ER1 ($T=77.3$ K, $t_{dw}=30$ min) and the results of the fitting procedure (solid line). (b) The intergrain current densities j_w calculated from these data within various approximations (see details in the text).

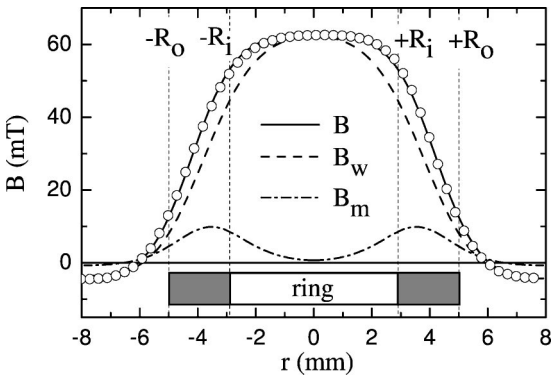

FIG. 10. The radial profile $B^{expt}(r)$ of the remanent flux density measured at $z=3$ mm above the center of the ring ER1 and its theoretical approximation $B^{calc}(r)$ obtained by adjusting parameters j_m and j_w. The best-fit values $j_m=22.3$ kA/cm^2 and $j_w=14.05$ kA/cm^2 ($f=0.63$) were used to calculate the profiles $B_w(r)$ and $B_m(r)$. Note that since the distance z is close to $z_0=2.97$ mm, $B_m(r=0)\approx 0$.

one more—viz., the distance X between the seed and center of the ring (see Table II). When prepared, each ring was carefully inspected with a view to avoid the cracks which could reduce the effective cross section $S=(R_o-R_i)2L$ and influence, thereby, the current distribution inside a ring.

In order to estimate the distribution of the currents flowing in entire rings at the remanent state, we duplicated the procedure described in Sec. III. Figure 9(a) presents the profile $B(r=0,z)$ measured along the axis of the ring ER1 (see Table II). One can, certainly, fit the whole profile $B(r=0,z)$ by selecting appropriate parameters j_m and f. The best fit is obtained at $j_m=21.43$ kA/cm^2 and $j_w=14.08$ kA/cm^2 [solid line in Fig. 9(a)]. There exists, though, an opportunity to determine the intergrain and intragrain currents separately. By substituting the flux densities $B(r=0,\pm z_0)$ into Eq. (13), one obtains quite similar results $j_w=14.0$ and 13.9 kA/cm^2 for the points $+z_0$ and $-z_0$, respectively. Estimation of the intragrain current density j_m seems a bit more complicated. Accepting j_w to be the average value 13.95 kA/cm^2, one can use Eq. (7) to restore the flux density $B_w(r=0,z)$ at arbitrary distance z (say, in the ring center, $z=0$). Then, by deducting this value $B_w(0,0)$ from the experimental one $B(0,0)$, one can extract the intragrain flux component, $B_m(0,0)$. Finally, one has to adjust the parameter f (or $j_m=j_w/f$) in Eq. (8) so as to approach the same remainder $B_m(0,0)$. Following this procedure, we obtained $f=0.645$ and $j_m=j_w/f=21.63$ kA/cm^2. The latter is in a reasonable agreement both with the previous estimate (21.43 kA/cm^2) and with the values (≈ 22.7 kA/cm^2) reported for the cut rings which also were carved from the central part of MT YBCO sample (see Table I). A similar procedure was applied to the other rings; the results are included in Table II. Let us, though, postpone their discussion until the next section.

Since any innovation assuredly needs a careful comparison with conventional methods, we paid special attention to this task. At first, we considered those techniques (see, for example, Refs. 9, 10, and (14)

$$B=\begin{cases} I_w/[2R], & \text{Approx. 1,} \\ I_w/[2(R^2+z^2)^{1.5}], & \text{Approx. 2,} \\ j_w\Phi(L,z,R_o,R_i), & \text{Approx. 3,} \end{cases} \tag{16}$$

which neglect the intragrain flux component B_m. Using each of the mentioned approximations, we calculated the intergrain current densities $j_w=I_w/[2L(R_o-R_i)]$ from the same experimental profile $B(r=0,z)$ and plotted these data in Fig. 9(b). It is worth to underline an evident similarity of the curves obtained within the Approx. 2 and 3 with those presented in Fig. 4(b). Their deviation from a nearly constant value j_w, which corresponds to the case when the intragrain currents are taken into account [Approx. 4 in Fig. 9(b)], make these methods suitable only for rough estimates even for relatively homogeneous rings like ER1 ($f\simeq 0.65$).

Then, we studied the same ring by an approach which is akin to that described in Ref. 10. Briefly, the radial profile $B(r,z=\text{const})$ in the remanent state ($T=77.3$ K, $t_{dw}=30$ min) was measured and fitted by adjusting two parameters j_w and j_m. The obtained data and their fit agree well with each other (see Fig. 10). One has also to mention that the shape of the intergrain flux component $B_w(r)$ noticeably differs from the shape of the experimental curve, $B(r)$. This example once more demonstrates how important the flux correction is due to the intragrain currents. However, yet more important, at the moment, is the good agreement between the best-fit parameters $j_w=14.05$ kA/cm^2 and $j_m=22.3$ kA/cm^2 ($f=0.63$) and their values estimated by the ''two-point'' method.

Concluding this section, we would like to emphasize the following. In order to know j_w and j_m, one no longer requires scanning the magnetic flux. Both values may, with a proper accuracy, be determined from *two* experimental data, e.g., $B(z_0)$ and $B(0)$. In contrast to any scanning techniques, this ''two-point'' method is quite applicable in a wide range

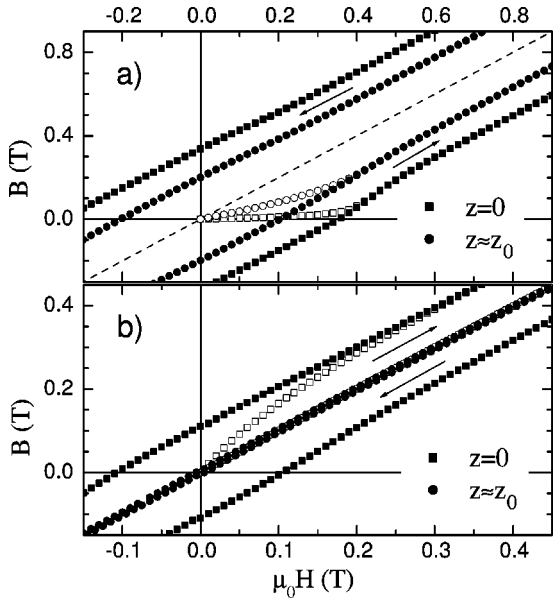

FIG. 11. The B vs H dependences ($T=77.3$ K, sweep rate 0.5 T/min) for the ring ER3 (a) without and (b) with the radial slit. The curves were measured at various heights $z=0$ and $z_0\approx3.3$ mm above the ring center.

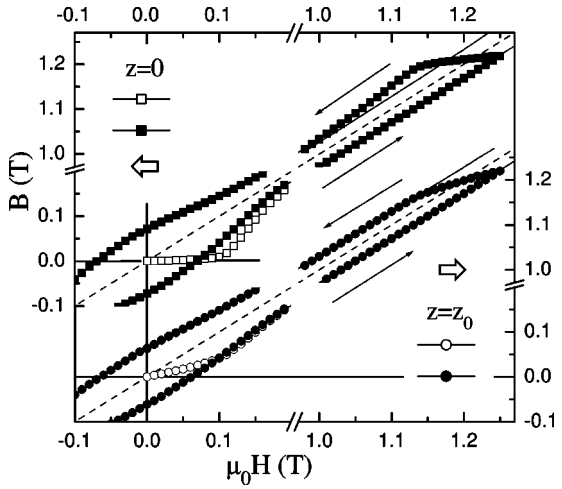

FIG. 12. The B vs H dependences ($T=77.3$ K, sweep rate 0.5 T/min) for the ring ER4. The data are measured at various heights $z=0$ and $z_0\approx3.15$ mm above the ring center. Solid lines (on the right side) correspond to the loops remagnetized at higher magnetic field $\mu_0H=1.5$ T. Note that the $B(z=0)$ anomalies during the field penetration (on the initial branch, $\mu_0H\approx0.12$ T, as well as on the descending field branch, near field reversal) are absent at the height $z=z_0$.

of magnetic fields and/or temperatures. This also has no evident restrictions for a time to start the measurements. Realizing these benefits, we used this approach for further studies.

C. Rings in external magnetic fields

Heretofore, we acquiesced in the Bean model which presumes that the critical current density remains independent of the external magnetic field H. Meantime, H is well known to reduce j_w. This reduction, in turn, can essentially worsen, say, the performance of superconducting devices constructed from welded grains. It is, therefore, vitally important to control the intergrain current I_w which flows through the weak link immersed in strong magnetic fields. Another task on which we are going to focus attention is the penetration of a magnetic flux into the rings. This process was recently shown[22] to be accompanied by a highly nonuniform current distribution. Although our approach describes mostly rings in the full-magnetized state, this allowed us to shed some light on this phenomenon.

Since the behavior of the rings enumerated in Table II *gradually* changed from the most homogeneous case ER3 ($f\simeq0.73$) to the most inhomogeneous one ER4 ($f\simeq0.41$), these were the samples which we selected for an illustration.

Figure 11 presents the B vs H dependences obtained at various heights $z=0$ and $z=3.3$ mm$\approx z_0$ above the center of the ring ER3 (a) before and (b) after we introduced therein the radial slit. Let us primarily discuss the flux penetration into a bore ($z=0$) of the zero-field-cooled (ZFC) ring in the nonmagnetized, virgin state (open symbols).

Figure 11(a) shows that the entire ring shields ($B=0$) its bore[36] by generating the circular current I_w which, at first, exactly compensates μ_0H. However, I_w is limited by its critical value. Thus, the field H_p, when the currents are no longer enough for full screening ($B>0$), may be used to estimate the critical current density j_w.

Penetration of the magnetic flux into a bore ($z=0$) of the cut rings seems absolutely different. Since there are no circular currents ($I_w=B_w=0$), the flux density is defined merely by the intragrain flux component B_m. For this reason, the initial curve $B(z=0)$ in Fig. 11(b) deviates from zero as soon as $H>0$. One can also observe that the initial slope dB/μ_0dH exceeds unity. In other words, the $B(z=0)$ loop in the cut rings and that in the entire rings have opposite widths $\Delta B=B-\mu_0H$ (Fig. 11). This behavior is reminiscent of the opposite components $B_m(z=0)<0$ and $B_w(z=0)>0$ of the remanent flux presented in Fig. 4. The B_m vs z dependences in Figs. 4 and 7 also explain why the loop $B(H)$ in the cut rings shrinks into the straight line $B=\mu_0H$ as z increases up to z_0 [see the respective curve in Fig. 11(b)] and, then, expands again with the negative width $\Delta B(z>z_0)<0$.

Extremely interesting anomalies (see Fig. 12) accompany the flux penetration into a bore ($z=0$) of the ring ER4, where the weakest link is really weak ($f\simeq0.41$) as compared with the rest of the ring material. In particular, the curve of the magnetic flux density $B(z=0)$ at the initial field branch (open squares) approaches the full-magnetized loop (solid squares) from outside; i.e., there exists a field range ($0.08\text{ T}\leqslant\mu_0H\lesssim0.5$ T) wherein the partially magnetized ring more effectively screens its bore than that in the full-magnetized state. Similar anomalies are also observed near the field reversal. Figure 12 shows these effects at $\mu_0H=1.25$ T; solid lines on the right side of Fig. 12 correspond to the loop reversed at a bit higher magnetic field $\mu_0H=1.5$ T. Since these anomalies almost disappear at the height $z=z_0$ (circles), one can preliminary conclude that

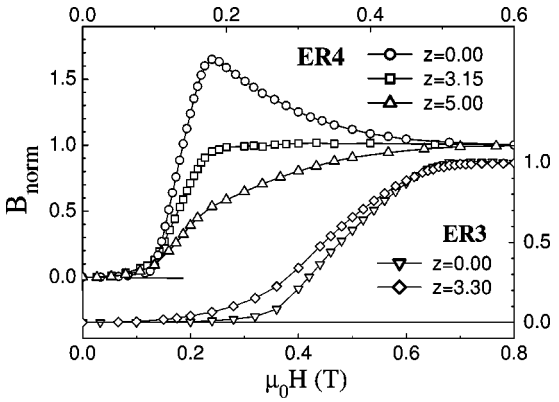

FIG. 13. The remanent flux density B vs the magnetic field $\mu_0 H$ at which the ZFC rings ER3 (right and bottom axes) and ER4 (left and top axes) were magnetized ($T=77.3$ K). The curves correspond to various distances $z=0$, $z=z_0$, and $z>z_0$ (given in mm), where the flux density was registered after the short dwell $t_{dw}=10$ s. Each curve is normalized to the full-penetration value obtained at $\mu_0 H=2$ T.

these are induced by changes in the distribution of the *intragrain* currents which correspond to the concentric, counterrotating current loops mentioned in Ref. 22.

To test this suggestion, we realized the following experiments. The samples were ZFC down to $T=77.3$ K and magnetized at this temperature in a certain field H. When a field was switched off, the remanent flux density was registered (after $t_{dw}=10$ s) at various heights above the ring center, $z=0$, z_0, and $z>z_0$. We repeated this procedure, gradually increasing H until the remanent flux density B approached its saturation. The obtained B vs $\mu_0 H$ dependences (normalized to the B values at $\mu_0 H=2$ T which well exceed the full-penetration field) are presented in Fig. 13. One can see that the flux density in the center of the weakly coupled ring ER4 (open circles) does exhibit a well-discernible maximum at $\mu_0 H=0.18$ T. A similar maximum was already observed in polycrystalline YBCO rings by Darhmaoui and Jung.[4] However, the concept of the Josephson vortex flow, which they invoked to unravel this phenomenon, can scarcely explain why the maximum totally disappears at larger distances $z=z_0$ and $z>z_0$ (respectively, squares and up triangles in Fig. 13).

To our opinion, both the maximum $B(z=0)$ in Fig. 13 and the $B(z=0)$ anomalies in Fig. 12 are of the same origin. Their reason becomes nearly obvious owing to the normalization trick used in Fig. 13. These phenomena occur since the full-penetration field $\mu_0 H_p \approx 0.5$ T (which is necessary to induce the whole currents) in the weakly coupled ring ER4 is much larger than the field $\mu_0 H_w \approx 0.2$ T wherein the intergrain current reaches its critical limit $j_w 2L(R_o-R_i)$ (squares in Fig. 12). So a further growth of the magnetic field ($H_w \leqslant H \lesssim H_p$) can generate merely the intragrain currents. Since the intragrain flux component B_m reverses its sign at the height $z=z_0$ [see, for example, Figs. 4, 7, or 11(b)], the increase of its amplitude has to result in an additional increment of the net flux density B measured at $z>z_0$ and—what we are going to prove—in its reduction when $z<z_0$. In other words, we believe that these anomalies become visible owing to demagnetizing effects. One more argument in favor of this scenario is that the ratio $H_w/H_p \simeq 0.4$ does appear very close to the parameter $f \simeq 0.41$. The same scenario is quite relevant for explication of the flux anomaly after field reversal.

Generally, a certain decrease of the remanent flux could also be explained by the sample heating due to viscous forces that are exerted on moving flux lines. Yet to attain the difference of 65% shown in Fig. 13, one usually needs the pulsed fields when the sweep rate is a few orders of magnitude faster[37] than that (0.5 T/min) used in our experiments. Another argument, which completely rejects the hypothesis of sample heating, is the absence of *any* $B(z=0)$ anomalies for the more homogeneous ring ER3 ($f \simeq 0.73$) which was measured at the same experimental conditions (Fig. 13). This absence may readily be explained by the following reasons. At first, the critical value of the intergrain current $I_w \sim f$ linearly grows with f and so does the flux component B_w which I_w produces. Since the intragrain current $I_m \sim (1-f^2)$ has an opposite tendency, the ratio B_m/B_w rapidly decreases as $f \to 1$. Finally, the larger f is, the closer the fields H_w and H_p become where, respectively, the intergrain and intragrain currents are saturated. Hence, the larger half ($\sim f$) of the intragrain flux component B_m appears *simultaneously* with the intergrain one ($H<H_w$) and only a small portion $\sim(1-f)$ does in the range $H_w \leqslant H \lesssim H_p$ where the B_m changes are not compensated by the B_w growth.

Thus, the closer is f to unity, the less pronounced have to be the $B(z=0)$ anomalies during the flux penetration. Studies of other rings (enumerated in Table II) confirm this statement. In particular, the difference between the maximum of the remanent flux $B(z=0)$ and its saturation value for the ring ER2 was registered to be 3.6% ($H_w/H_p=0.6 \approx 0.52=f$). For the rings ER1 and ER3 with $f \simeq 0.65$ and $f \simeq 0.73$, respectively, this value did not exceed the experimental error ($\approx 0.3\%$). On the other hand, one can conclude—be the conclusion ever so amazing—that the remanent flux density $B(z<z_0)$ of weakly coupled rings ($f \to 0$) may totally vanish or even become negative [note, for example, a negative remanence of ≈ -0.1 T in the center of the cut ring ER3 shown in Fig. 11(b)] as the magnetizing field ascends.

Let us yet come back to an estimation of the intergrain and intragrain current densities in external magnetic fields. As mentioned above, our approach requires removing the constant background $\mu_0 H$ from the experimental data, $B(z=0)$ and $B(z=z_0)$, in the full-magnetized state [solid points in Figs. 11(a) and 12]. This task may conveniently be resolved by calculating the half-difference between the descending, $B_\downarrow$, and the ascending, $B_\uparrow$, field branches:

$$\Delta B(H)=[B_\downarrow(H)-B_\uparrow(H)]/2. \tag{17}$$

Then, by applying the "two-point" method to each pair of the points, $\Delta B(H)|_{z=0}$ and $\Delta B(H)|_{z=z_0}$ presented in Fig. 14(a), we restored the sought $j_w(H)$ and $j_m(H)$ dependences as well as their ratio $f(H)$ which also was found to depend on H. Moreover, the weaker the link, the more sensitive this appeared to external magnetic fields [see Fig. 14(c)]. In par-

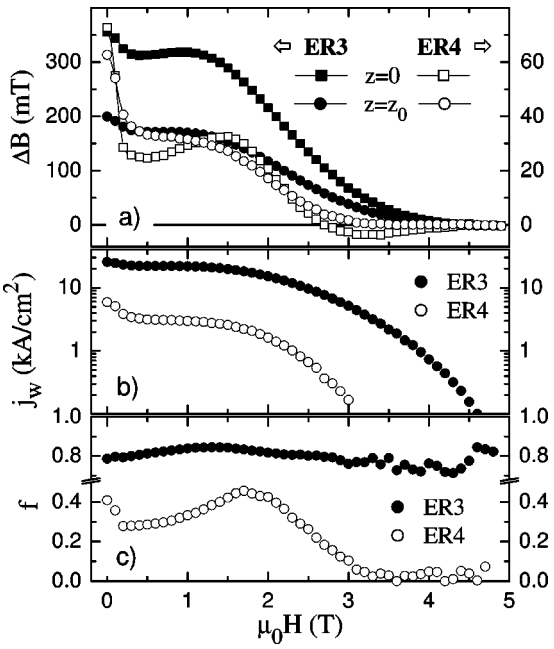

FIG. 14. (a) The half-width $\Delta B(H)$ of the flux density loops shown in Figs. 11(a) and 12. The field dependences (b) $j_w(H)$ and (c) $f(H)$ are calculated from the $\Delta B(H)$ data.

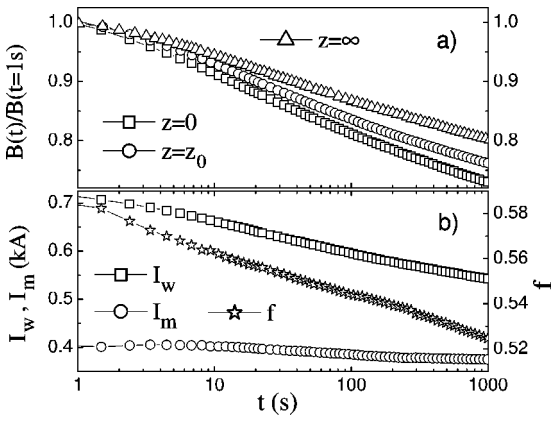

FIG. 15. (a) Dissipation of the remanent flux density $B(t)$ measured at various heights z above the center of the ring ER2 ($T=77.3$ K). The curve $z=\infty$ corresponds to the time changes of the remanent magnetic moment m. (b) The intergrain and intragrain currents I_w and I_m as well as the parameter $f=j_w/j_m$ which are restored from these data.

ticular, in contrast to the sample ER3 which values f cluster around 0.8, the curve $f(H)$ in the ring ER4 exhibits two well-defined maxima. Their origin may be attributed to the strongly coupled channels in GB's with a low misorientation angle.[33–35] It is suggested[33,34] that small magnetic fields *partially* decouple a weak link; i.e., there exists a secondary, non-weak-linked component of the intergrain conduction. Such channels of relatively undisturbed crystal lattice (i.e., microbridges of the intrinsic, intragranular material which occupy only a small area of the GB surface) were directly confirmed by the transmission electron microscopy of the 10°-bicrystal YBCO film.[35] Following this multifilamentary model, one can identify the saddle point between the two mentioned maxima as the field which decouples the weakest link, but still does not influence the other weak links, restricting the intragrain current I_m given by Eq. (3). So a further increase of field reduces mostly the intragrain current density $j_m(H)$ and, hence, results in a second peak of the $f(H)$ dependence. More interesting is that the same sequence seems valid for high fields H_{irr} which totally decouple weak links by breaking their strongly coupled channels. Figure 14(c) shows that this decoupling first happens with the weakest link $\mu_0 H_{irr} \approx 3.3$ T and, then, with the rest of the weak links (≈ 4.6 T) in the ring ER4. In other words, within the range $3.3\ \mathrm{T} \lesssim \mu_0 H \lesssim 4.6\ \mathrm{T}$ there is already no circular current ($f=0$), but the intragrain currents, which result in $B_m<0$, still continue to flow. It is the reason why the half-width $\Delta B(H)|_{z=0}$ [open squares in Fig. 14(a)] alters its sign. To our knowledge, only this type of measurement opens up the opportunity to see this high-field phenomenon.

Finalizing this section, one has to mention some discrepancies between the parameters $f(H=0)$ extracted from the magnetization cycle data [Fig. 14(c)] and those which were registered after a long dwell (see Table II). Comparing these values, we took cognizance of a weak tendency for f to decrease with time. This question, though, is worthy of a separate discussion.

D. Dissipation of the magnetic flux

It is well known that thermoactivated vortices ($T>0$) can leave the pinning centers under the Lorentz force[38]

$$F_L = V\frac{B}{\mu_0}\frac{dB}{dr}. \tag{18}$$

Such motion of the vortex lines is equivalent to the resistance to a current and responsible for the power dissipation. For this reason, we were not surprised that the absolute values of the intergrain and intragrain current densities were found to decrease during a dwell. Meanwhile, their ratio f was also suspected to depend on time. If this tendency does exist, the flux depinning processes may noticeably falsify a genuine ability f of weak links to transmit current. It is therefore very important to know to what extent we can rely on the previous data obtained by scanning Hall-sensor magnetometry[8–15] which *a priori* requires a long-continued dwell.

At first, we more carefully explored the intergrain and intragrain flux losses and their influence on the current distribution. Figure 15(a) shows the time dependences of the remanent flux density measured at various heights $z=0$, z_0, and ∞ above the center of the ring ER2. These curves [normalized, for convenience, to their values $B_0=B(t=1\ \mathrm{s})$] neatly indicate that the relative dissipation rate

$$S=-\frac{1}{B_0}\frac{dB(t)}{d\log t} \tag{19}$$

gradually decreases with distance z from the sample. This decrease does prove that the intergrain current I_w is dissipated faster than the intragrain one I_m. Using the "two-

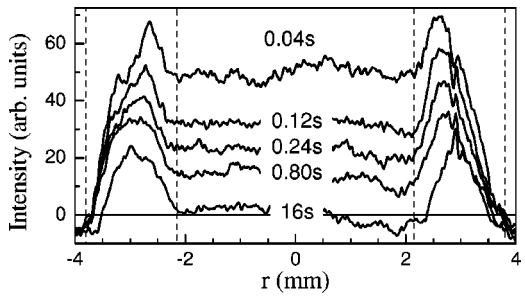

FIG. 16. Radial profiles of the remanent flux density $B(r,z)$ on the surface $z=\pm L$ of the ring ER2 at various dwell times (in seconds). The data were obtained by the magneto-optical imaging technique ($T=81$ K).

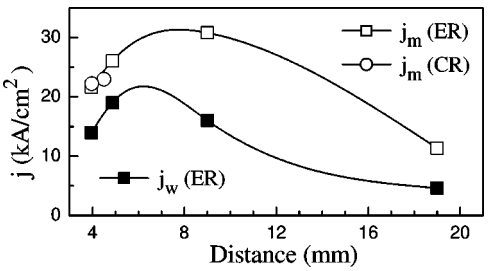

FIG. 17. The intergrain and intragrain current densities inside the MT YBCO crystal vs the distance from the seeding point. For those rings which are carved from the central part of the crystal, the distance is taken equal to their average radius $(R_o+R_i)/2$. The data are compiled from measurements of both the entire rings (ER) and the cut ones (CR).

point'' procedure, we confirmed this qualitative conclusion by the numerical values I_w and I_m [Fig. 15(b)]. The intergrain current decay S was determined to be 8.2% per time decade, whereas S for the intragrain current did not exceed 2%. Consequently, each sequent time decade reduced the parameter f to 0.021.

There may be several reasons which explain this phenomenon. The most evident one is that the intragrain current loop does not cross the weakest link where the largest losses are expected. One can also attribute this effect to the Lorentz force (18) which, in accordance with the radial distribution $B(r)$ [see Fig. 2(a)], more effectively stimulates a motion of the flux vortices trapped near the inner periphery ($R_c<r<R_i$) of the ring. This question will be the subject of the next studies.

Whatever the genuine reasons are, these do result in a spatial redistribution ($f\neq$const) of the currents during a dwell. This redistribution passes the faster the faster the flux creep is itself. One can conclude that at low temperatures and small magnetic fields, slow experimental methods may still give a reasonable approximation for the parameter f describing the current limiting properties of the weak link. Otherwise, the long-continued dwell is absolutely inadmissible and so, unfortunately, is the *scanning* Hall-sensor method, which provides another way to discern between the intergrain and intragrain currents.[10] In order to visualize how appallingly large the error just after a few seconds of dwell may become, we investigated the remanent flux creep in the same ring ER2 at higher temperature $T=81$ K. In view of the extremely sharp decay, it was necessary to use the magneto-optical image technique[27] which allowed us to register the flux changes much faster than other methods. So the ring was cooled down to 81 K, isothermally magnetized, and, then, the magnetic field was rapidly (during a delay 0.04 s between neighboring image frames) switched off. Figure 16 clearly shows that the flux inside the ring bore $|r|<2.15$ mm (dashed lines)—i.e., that which is induced by the intergrain (circular) current I_w—rapidly decreases with time and so does the parameter f.

V. SUMMARY

We explored the intergrain and intragrain currents flowing in bulk MT YBCO samples containing weak links.

To perform these studies, we developed a simple, reliable, and nondestructive method which allows us to discern between these types of current. In particular, we showed that, if a sample has the shape of a ring with finite size, the intragrain current (because of demagnetizing effects) gives an alternating-sign contribution B_m to the net flux density B; viz., B_m is negative near the ring center and positive at large distances. We also considered the points $z=\pm z_0$, wherein the ring axis ($r=0$) intersects the border ($B_m=0$) between these areas, and demonstrated that the distance z_0 appears almost independent of the current distribution. Hence, positioning the Hall sensor at a height $\pm z_0$ above (or below) the ring center, one can measure the ''pure'' intergrain flux component B_w and estimate the intergrain (circular) current which produces B_w. This—the so-called ''one-point'' method—seems very promising for the characterization of a quality of superconducting welds. In this case, the numerical calculations of the distance z_0 may optionally be replaced by its direct measurement preceding the welding procedure. The same idea may, in the future, be extended to less exotic sample shapes—for example, for finite-size slabs.

By measuring the flux density $B(r=0,z)$ in one more point $z\neq z_0$, one can also restore the intragrain current I_m. We showed that it is the current which is responsible for very unusual phenomena registered near the center ($r=0,z=0$) of weakly coupled rings ($f<0.5$). In particular, we observed (see Figs. 12 and 13) that, being in a partially penetrated state, such rings screen their bores more effectively than those after the full flux penetration. A similar situation was registered after field reversal at relatively high fields (Fig. 12). We also revealed an absolutely irregular situation when, owing to the destruction of the strongly coupled channels[33–35] in the weakest link, the magnetic fields $H\geqslant H_{irr}$ result in a negative screening of the ring bore [Fig. 14(a)]. The dependence of the flux dissipation rate S on a distance z from the ring [Fig. 15(a)] could also be scarcely explicable unless the intragrain current I_m is taken into account. These effects are merely the first items in a large list of somewhat ''strange'' effects (both already published and still waiting for publication) in finite-size superconducting rings and/or hollow cylinders. We believe that, by presenting a method which allows one to estimate I_w and I_m,

this work opens new perspectives to reveal and explain other items.

Concluding the paper, we would like to touch on the superconducting welding again. Unless the welding techniques give a totally reproducible quality of joints, one has to minimize their number by welding the bulk MT crystals which are as large as possible. Their sizes, though, are severely restricted because of a degradation of the superconducting properties from the seeding point toward the crystal rims (see Fig. 17). There exists, therefore, an optimum welding size—i.e., the size at which the rims of welded parts may transmit the same density of current as that which can flow across their joint. Since, at present, the best joints are reported to carry currents with a density of ≈ 10 kA/cm^2, we believe that the welding technology should be developed mostly for joining of relatively large, 25×25 mm^2 MT YBCO blocks.

ACKNOWLEDGMENTS

This work was supported by the German BMBF under Project No. 13N6854A3, the Russian Foundation for Basic Research (Project No. 02-02-17062), and INTAS (Project No. 02-2282). One of the authors (A.B.S.) would like to thank R. Hiergeist for useful discussions.

*Author to whom correspondence should be addressed. On leave from Institute for Magnetism, Kiev, Ukraine. Electronic address: surzhenko@ipht-jena.de

[1] P. Leiderer and R. Feile, Z. Phys. B: Condens. Matter **70**, 141 (1988).
[2] M.A.-K. Mohamed and J. Jung, Phys. Rev. B **44**, 4512 (1991).
[3] J. Jung, I. Isaac, and M.A.-K. Mohamed, Phys. Rev. B **48**, 7526 (1993).
[4] H. Darhmaoui and J. Jung, Phys. Rev. B **53**, 14 621 (1996).
[5] S. Jin, T.H. Tiefel, R.C. Sherwood, M.E. Davis, R.B. van Dover, G.W. Kammlott, R. Fastnacht, and H.D. Keith, Appl. Phys. Lett. **52**, 2074 (1988).
[6] M.J. Sturm, Z.A. Chaudury, and S.A. Akbar, Mater. Lett. **12**, 316 (1991); K. Salama and V. Selvamanickam, J. Appl. Phys. **60**, 898 (1992).
[7] D. Shi, Appl. Phys. Lett. **66**, 2573 (1995).
[8] Ph. Vanderbemden, A.D. Bradley, R.A. Doyle, W. Lo, D.M. Astill, D.A. Cardwell, and A.M. Campbell, Physica C **302**, 257 (1998).
[9] H. Zheng, M. Jiang, R. Nikolova, U. Welp, A.P. Paulikas, Yi Huang, G.W. Crabtree, B.W. Veal, and H. Klaus, Physica C **322**, 1 (1999).
[10] H. Zheng, H. Claus, L. Chen, A.P. Paulikas, B.W. Veal, B. Olsson, A. Koshelev, J. Hull, and G.W. Crabtree, Physica C **350**, 17 (2001).
[11] T. Prikhna, W. Gawalek, V. Moshchil, A. Surzhenko, A. Kordyuk, D. Litzkendorf, S. Dub, V. Melnikov, A. Plyushchay, N. Sergienko, A. Koval, S. Bokoch, and T. Habisreuther, Physica C **354**, 333 (2001).
[12] M.P. Delamare, H. Walter, B. Bringmann, A. Leenders, and H.C. Freyhardt, Physica C **329**, 160 (2000).
[13] C. Harnois, G. Desgardin, and X. Chaud, Supercond. Sci. Technol. **14**, 708 (2001).
[14] T. Puig, P. Rodriguez, Jr., A.E. Carillo, X. Obradors, H. Zheng, U. Welp, L. Chen, H. Claus, B.W. Veal, and G.W. Crabtree, Physica C **363**, 75 (2001).
[15] J. Yoshioka, K. Iida, T. Negichi, N. Sakai, K. Noto, and M. Murakami, Supercond. Sci. Technol. **15**, 712 (2002).
[16] J.G. Noudem, E.S. Reddy, M. Tarka, M. Noe, and G.J. Schmitz, Supercond. Sci. Technol. **14**, 363 (2001).
[17] H. Walter, Ch. Jooss, F. Sandiumenge, B. Bringmann, M.P. Delamare, A. Leenders, and H.C. Freyhardt, Europhys. Lett. **55**, 100 (2001).
[18] H. Claus, U. Welp, H. Zheng, L. Chen, A.P. Paulikas, B.W. Veal, K.E. Gray, and G.W. Crabtree, Phys. Rev. B **64**, 144507 (2001).
[19] A.A. Kordyuk, V.V. Nemoshkalenko, A.I. Plyushchay, T.A. Prikhna, and W. Gawalek, Supercond. Sci. Technol. **14**, L41 (2001).
[20] M. Kambara, N. Hari Babu, D.A. Cardwell, and A.M. Campbell, Physica C **372–376**, 1155 (2002).
[21] M. Murakami, Supercond. Sci. Technol. **13**, 448 (2000).
[22] M. Pannetier, F.C. Klaassen, R.J. Wijngaarden, M. Welling, K. Heeck, J.M. Huijbregtse, B. Dam, and R. Griessen, Phys. Rev. B **64**, 144505 (2001).
[23] A.B. Surzhenko, M. Zeisberger, T. Habisreuther, D. Litzkendorf, and W. Gawalek, Supercond. Sci. Technol. **15**, 1353 (2002).
[24] C.D. Dewhurst, Wai Lo, Y.H. Shi, and D.A. Cardwell, Mater. Sci. Eng., B **53**, 169 (1998).
[25] D. Litzkendorf, T. Habisreuther, M. Wu, T. Straßer, M. Zeisberger, W. Gawalek, M. Helbig, and P. Görnert, Mater. Sci. Eng., B **53**, 75 (1998).
[26] Th. Klupsch, Th. Straßer, T. Habisreuther, W. Gawalek, S. Gruss, H. May, R. Palka, and F.J. Mora Serrano, J. Appl. Phys. **82**, 3035 (1997).
[27] L.S. Uspenskaya, V.K. Vlasko-Vlasov, V.I. Nikitenko, and T.H. Johansen, Phys. Rev. B **56**, 11 979 (1997).
[28] L.S. Uspenskaya, I.G. Naumenko, G.A. Emelchenko, Yu.B. Bugoslavskii, S.A. Zver'kov, E.B. Yakimov, D. Litzkendorf, W. Gawalek, and A.D. Caplin, Physica C **390**, 127 (2003).
[29] P. Diko, Supercond. Sci. Technol. **13**, 1202 (2000).
[30] A.B. Surzhenko, S. Schauroth, M. Zeisberger, T. Habisreuther, D. Litzkendorf, and W. Gawalek, Physica C **372-376**, 1212 (2002).
[31] C. Kim, H.G. Lee, K.B. Kim, and G.W. Hong, J. Mater. Res. **10**, 1605 (1995).
[32] Whether the vortex pinning by Y211 inclusions is due to the pure interfacial mechanism [see *Melt Processed High-Temperature Superconductors*, edited by M. Murakami (World Scientific, Singapore, 1992)] or to the YBCO dislocations which surround the embraced Y211 inclusions [K. Salama and D.F. Lee, Supercond. Sci. Technol. **7**, 177 (1994)] is still ambiguous.
[33] D. Dimos, P. Chaudhari, J. Mannhart, and F.K. LeGoues, Phys. Rev. Lett. **61**, 219 (1988); D. Dimos, P. Chaudhari, and J. Man-

nhart, Phys. Rev. B **41**, 4038 (1990).
[34] M.F. Chisholm and S.J. Pennycock, Nature (London) **351**, 47 (1991).
[35] N.F. Heinig, R.D. Redwing, I. Fei Tsu, A. Gurevich, J.E. Nordman, S.E. Babcock, and D.C. Larbalestier, Appl. Phys. Lett. **69**, 577 (1996).
[36] Similar behavior in conventional, low-temperature superconductors was described by W. Buckel, *Superconductivity: Fundamentals and Applications* (VCH, Weinheim, 1991), p. 173.
[37] A.B. Surzhenko, S. Schauroth, M. Zeisberger, T. Habisreuther, D. Litzkendorf, and W. Gawalek, Supercond. Sci. Technol. **14**, 770 (2001).
[38] See, for example, A. Gurevich and E.H. Brandt, Phys. Rev. Lett. **73**, 178 (1994).
[39] Numerical methods (e.g., the bisectional search) determine the roots $\pm z_0$ of Eq. (12) to any desired accuracy. For this reason, we desisted from attempts to reduce Eq. (12) into an absolute form $z_0 = f(R_i, R_o, L)$ which can be obtained by introducing further restrictions for the ring geometry.
[40] Owing to the finite height of real rings, the requirement for the ratio R_o/R_i is actually yet less stringent.